Article

Crystal Design and Photoactivity of TiO$_2$ Nanorod Template Decorated with Nanostructured Bi$_2$S$_3$ Visible Light Sensitizer

Yuan-Chang Liang *, Shao-Yu You and Bo-Yue Chen

Department of Optoelectronics and Materials Technology, National Taiwan Ocean University,
Keelung 20224, Taiwan
* Correspondence: yuanvictory@gmail.com

Abstract: In this study, TiO$_2$-Bi$_2$S$_3$ composites with various morphologies were synthesized through hydrothermal vulcanization with sputtering deposited Bi$_2$O$_3$ sacrificial layer method on the TiO$_2$ nanorod templates. The morphologies of decorated Bi$_2$S$_3$ nanostructures on the TiO$_2$ nanorod templates are controlled by the duration of hydrothermal vulcanization treatment. The Bi$_2$S$_3$ crystals in lumpy filament, nanowire, and nanorod feature were decorated on the TiO$_2$ nanorod template after 1, 3, and 5 h hydrothermal vulcanization, respectively. Comparatively, TiO$_2$-Bi$_2$S$_3$ composites with Bi$_2$S$_3$ nanowires exhibit the best photocurrent density, the lowest interfacial resistance value and the highest photodegradation efficiency towards Rhodamine B solution. The possible Z-scheme photoinduced charge separation mechanism and suitable morphology of Bi$_2$S$_3$ nanowires might account for the high photoactivity of TiO$_2$ nanorod-Bi$_2$S$_3$ nanowire composites.

Keywords: composites; vulcanization; photoactivity

1. Introduction

Nanorod arrays of TiO$_2$ are beneficial to provide direct channels for electron transport, reducing the recombination probability of electrons in the transmission process. The rod morphology helps to improve the electron injection and collection efficiency of TiO$_2$ semiconductor [1–5]. However, the wide band gap nature of TiO$_2$ engenders poor response to visible light [6,7]. In order to improve the photoactivity of TiO$_2$, the strategy of semiconductor coupling is often used to enhance the solar energy conversion and utilization of TiO$_2$ [8]. Several cases of TiO$_2$ coupled with a visible light sensitizer has been shown a promising approach to improve solar energy utilization efficiency. TiO$_2$ microspheres coupled with CdS nanoparticles enhance the light harvesting ability and suppress the electron-hole recombination of TiO$_2$ and CdS [9]. The electrospinning formed TiO$_2$/CuO composite nanofibers enhance light absorbance and interparticle charge transfer and lower the band gap energy, thus promoting absorbance and utilization of photon energy from a broader light spectrum [10]. Precise control of Bi$_2$O$_3$ coverage layer phase composition realizes the high photoactivity of the one-dimensional TiO$_2$-Bi$_2$O$_3$ composites [11]. The decoration of ZnFe$_2$O$_4$ crystallites onto TiO$_2$ improves the photoactivity of TiO$_2$ and enhance the photodegradation performance towards Methylene orange [12]. The TiO$_2$/Bi$_2$S$_3$ core–shell nanowire arrays demonstrate improved photocurrent density than that of pristine TiO$_2$ because of the broadened light absorption ability and the increased charge carrier separation efficiency [13]. Similarly, Bi$_2$S$_3$ nanowires/TiO$_2$ nanorod arrays exhibit an excellent photoelectrochemical activity [14]. Rosette-rod TiO$_2$/Bi$_2$S$_3$ shows substantial improvement in photoresponse in compared with pristine TiO$_2$ photoanode [15]. Furthermore, hydrothermal method deposition of TiO$_2$/Bi$_2$S$_3$ composite film is presented to be promising for applications of photoanode [16]. These examples clearly present the feasibility of construction of TiO$_2$-Bi$_2$S$_3$ heterogeneous system to be used in photoactive devices with an improved efficiency.

Among various visible-light sensitizers, Bi_2S_3 has attracted much attention because it is environmentally friendly and non-toxic. Bi_2S_3 has a high optical absorption coefficient and a suitable band gap, which can absorb most of the visible light spectrum [17]. Bi_2S_3 crystals with a large area growth and different morphologies have been realized through various chemical routes [18]. The photoactivity of Bi_2S_3 crystals is highly dependent on shape, size, and crystalline quality. How to precisely control the microstructures of Bi_2S_3 in order to fabricate TiO_2-Bi_2S_3 composites with satisfactory photoactivity is an important issue. In this study, Bi_2S_3 crystals with various microstructures were decorated on TiO_2 nanorod arrays via vulcanization of Bi_2O_3 sacrificial layer. The vulcanization of metal oxide to obtain metal sulfide has been shown to be a promising and easy approach to synthesize the metal sulfides with controllable microstructures [17,19]. Using metal oxide sacrificial layer to form the metal sulfide through vulcanization is an easy approach to control the microstructure of the as-synthesized metal sulfide. This approach is suitable for microstructural control of the sulfide crystals and thus tuning the physical properties of the samples. However, studies on synthesis of TiO_2-Bi_2S_3 composites through vulcanization of Bi_2O_3 layer and their photoactivities are lacking. A detailed vulcanization process-dependent microstructure evolution and photoactive properties of TiO_2-Bi_2S_3 composites are proposed in this study to realize the design of TiO_2-Bi_2S_3 composites with high photoactive performance.

2. Experiments

The synthesis of TiO_2 nanorod template on the F-doped SnO_2 (FTO) substrate was realized through a hydrothermal method at 170 °C. Other detailed parameters and preparation procedures have been described elsewhere [4]. The Bi_2O_3 thin films were sputter deposited on the TiO_2 nanorod template using a radio-frequency magnetron sputtering system. A metallic Bi disc was used as the target (99.9 wt%, 2 inches in diameter); the substrate temperature was fixed at 410 °C. The working atmosphere is mixed Ar/O_2 with a ratio of 1/1, the working pressure is 20 mtorr and sputtering power is 30 W. The sputtering duration is 50 min. The Bi_2O_3 thin-film coated TiO_2 nanorod templates are further immersed in a 20 mL reaction solution containing 0.1M thiourea and sealed in a Teflon-lined autoclave for a hydrothermal reaction at 160 °C for 1, 3, and 5 h to obtain TiO_2-Bi_2S_3 composites (named as BT-1, BT-3, and BT-5, respectively.).

Crystallographic structures of as-synthesized samples were investigated by X-ray diffraction (XRD) analysis using Cu Kα radiation with a two-theta scan range of 20–60° and scan rate of four degrees per min. The morphologies of the as-synthesized samples were investigated using a field emission scanning electron microscopy (FE-SEM). The morphology, high resolution images, crystallographic structure, and composition of BT-1 and BT-3 composite samples were investigated by high-resolution transmission electron microscopy (HR-TEM). X-ray photoelectron spectroscopy (XPS) was used to analyze the elemental binding energies of the as-synthesized samples. The diffuse reflectance spectra of the as-synthesized samples were recorded by using UV-vis spectrophotometer (Jasco V750) at the wavelength range of 200–800 nm. Photoelectrochemical (PEC) and electrochemical impedance spectroscopy (EIS) properties of various photoanodes were investigated using the potentiostat (SP150, BioLogic, Orlando, FL, USA). During measurements, an Ag/AgCl electrode were used as the reference electrode herein. The 0.5 M Na_2SO_4 solution was used as electrolyte and the light irradiation source for measurements is excited from 100 W Xe arc lamp. The 10 mL RhB solution (5×10^{-5} M) was used as target dye solution for photodegradation experiments. The RhB solution containing various photocatalysts with different irradiation durations (0, 15, 30, 45, and 60 min) was carried out to understand the photocatalytic activity of various as-synthesized samples.

3. Results and Discussion

The morphology of initial pristine TiO_2 rod array template was clearly observed from the SEM images in Figure 1a. As seen, the TiO_2 rods are uniformly grown on the entire substrate; moreover, TiO_2 rods have a regular cross-section and the side-wall surfaces are

smooth. Figure 1b displays the morphology of BT-1. A large number of lumpy filament-like crystals are covered on the top region of the TiO_2 rod template. Figure 1c shows that abundant nanowires with around 0.8 μm length were grafted on the TiO_2 rod template for the BT-3 sample. Such a morphology is similar to that of Bi_2S_3 nanowire-decorated TiO_2 rod heterostructures synthesized via a facile two-step hydrothermal growth process reported by Liu et al. [14]. Compared to Figure 1c, after extending the hydrothermal duration to 5 h, the diameter of one dimensional Bi_2S_3 thickened, and the length increases from 0.8 μm to 1.2 μm as exhibited in Figure 1d. Some aggregations of one-dimensional Bi_2O_3 crystals appear on the TiO_2 rod template. It has been shown that Bi_2O_3 oxide layer is easily etched and transfer to Bi_2S_3 phase during a vulcanization process with sulfur ions in the reaction solution [20].
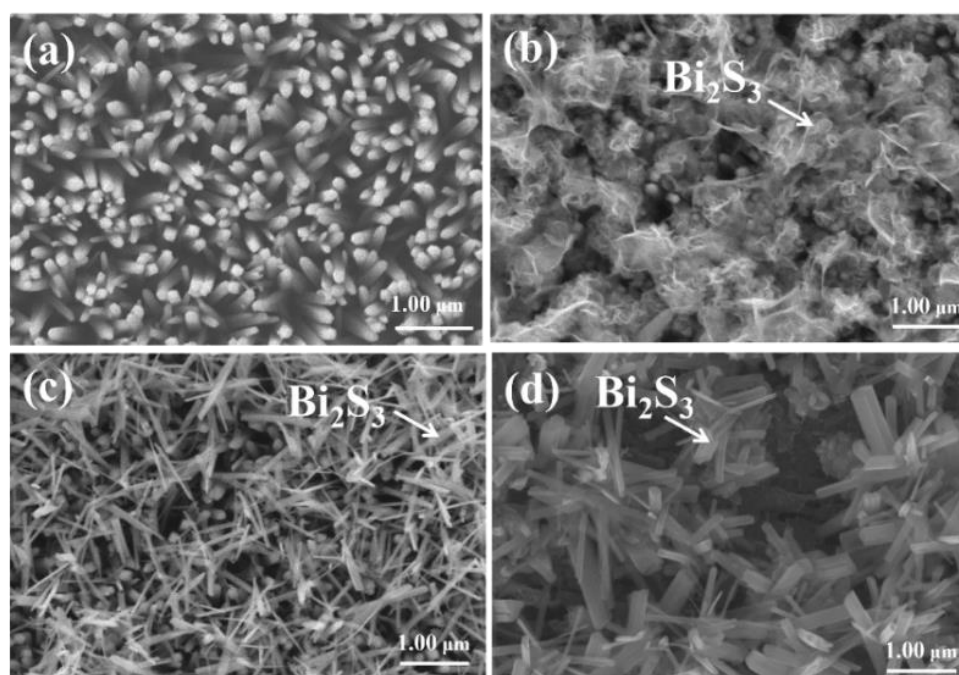
Figure 1. SEM images: (**a**) TiO_2 template, (**b**) BT-1, (**c**) BT-3, and (**d**) BT-5.

Figure 2 shows the possible formation processes of Bi_2S_3 nanostructures on the TiO_2-Bi_2O_3 composite rod template via different vulcanization processes in this study. Notably, in aqueous solution the solubility of Bi_2S_3 is much lower than that of Bi_2O_3. When the TiO_2-Bi_2O_3 composite rods are placed in a reaction solution containing a large amount of S^{2-} ions, there is a high possibility of S^{2-} ions transfer toward to the Bi_2O_3 surface as exhibited in (a). Furthermore, due to solubility disparity, the formation of Bi_2S_3 nuclei on Bi_2O_3 will occur during the vulcanization process because of the ion exchange of S^{2-} from the sulfur precursor solution and O^{2-} from the Bi_2O_3 surface. The generation of Bi_2S_3 crystals will continually proceed with a result of Bi^{3+} reacting with S^{2-} as exhibited in schematic (b). Further extending reaction duration, the Bi_2S_3 nuclei will slowly stack up to form loose filament structure at the given vulcanization condition of schematic (c). When an increase of the vulcanization reaction duration to 3 h, the loose and lumpy Bi_2S_3 clusters will transfer into abundant, distinguishable, and separable nanowire crystals covered on the TiO_2 template as displayed in schematic (d). When the reaction duration reaches 5 h, the one-dimensional Bi_2S_3 crystals continue to aggregate into a thicker rod structure, as shown in schematic (e).
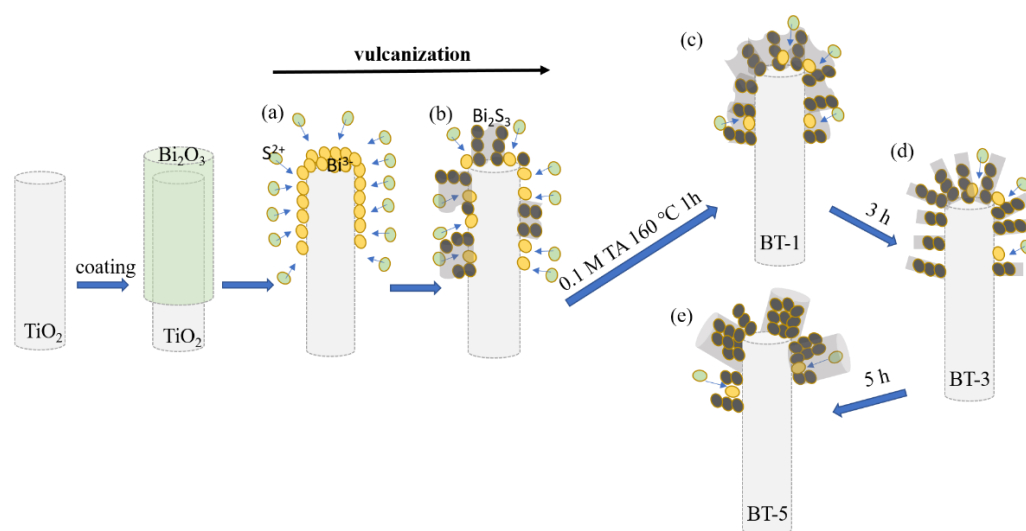
Figure 2. Schematic illustration of the formation processes of Bi_2S_3 nanostructures.

Figure 3a–c demonstrate the XRD patterns of vulcanization-treated BT-1, BT-3, and BT-5 samples. In addition to the Bragg reflections originated from the FTO substrate, the characteristic diffraction peaks centered at approximately 26.61°, 36.18°, and 54.76° can be indexed to (110), (101), and (211) planes of rutile TiO_2 (JCPDS No. 00-021-1276), revealing high crystallinity of the TiO_2 template. Notably, after hydrothermal vulcanization, several visible Bragg reflections originated from orthorhombic Bi_2S_3 phase could be clearly observed (JCPDS No. 017-0320) in the BT-1, BT-3, and BT-5 samples. Figure 3a–c present that addition of thiourea in hydrothermal reaction solution can vulcanize the Bi_2O_3 sacrificial oxide layer to transfer into the corresponding sulfide phase in BT-1, BT-3, and BT-5. The prolonged vulcanization process (from 1 to 5 h) improves Bragg reflection intensity of Bi_2S_3 phase of the samples, revealing an improved crystallinity of the samples. This might be associated with crystal morphology transformation of the loose and lumpy filament-like Bi_2S_3 crystals of BT-1 to one-dimensional Bi_2S_3 rods of BT-5 with prolonged vulcanization process. No Bragg reflections associated with Bi_2O_3 and other impurity phases were detected in the XRD patterns, revealing the vulcanization processes herein successfully synthesized the TiO_2-Bi_2S_3 composite structure, and the as-synthesized composite structures are crystalline.

Figure 4a shows the low-magnification TEM image of the BT-1. It can be observed that Bi_2S_3 flakes decorated on the TiO_2 rod. Figure 4b is the HRTEM image taken from the red square in Figure 3a. The distinct lattice fringes with a distance of approximately 0.28 nm are from the interplane spacing of orthorhombic Bi_2S_3 (2 2 1) and the lattice fringes with a spacing of 0.33 nm are from the interplane spacing of tetragonal TiO_2 (1 1 0). Figure 4c showed the selected area electron diffraction (SAED) pattern of several BT-1. Several clear diffraction spots arranged in centric rings are associated with the orthorhombic Bi_2S_3 (2 1 1), (2 2 1), and (4 3 1) planes and the rutile TiO_2 (1 1 0) plane, which agrees with the result observed by XRD analysis. This demonstrates the well-constructed TiO_2-Bi_2S_3 heterogeneous structure of BT-1, and a good crystallinity of the composites. The EDS spectrum in Figure 4d shows Ti, O, Bi, and S are the main elements in this composite structure. Furthermore, the particular element line scan intensity distributions displayed in Figure 4e reveals the construction of Bi_2S_3 flakes on the TiO_2 rod for the BT-1.
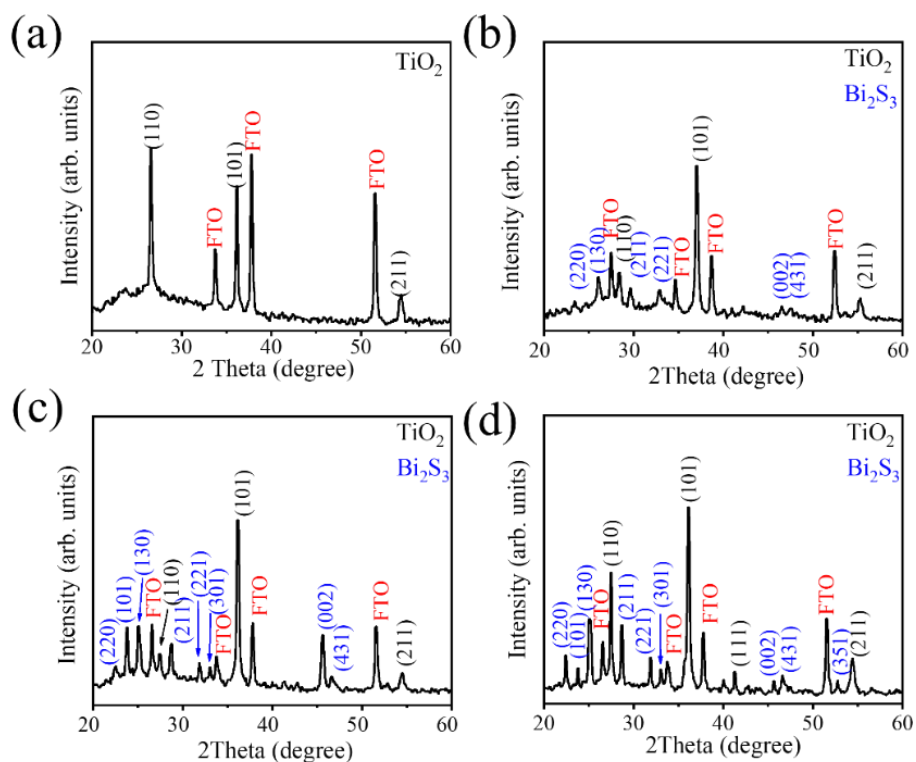
Figure 3. XRD patterns: (**a**) TiO$_2$ template, (**b**) BT-1, (**c**) BT-3, and (**d**) BT-5.
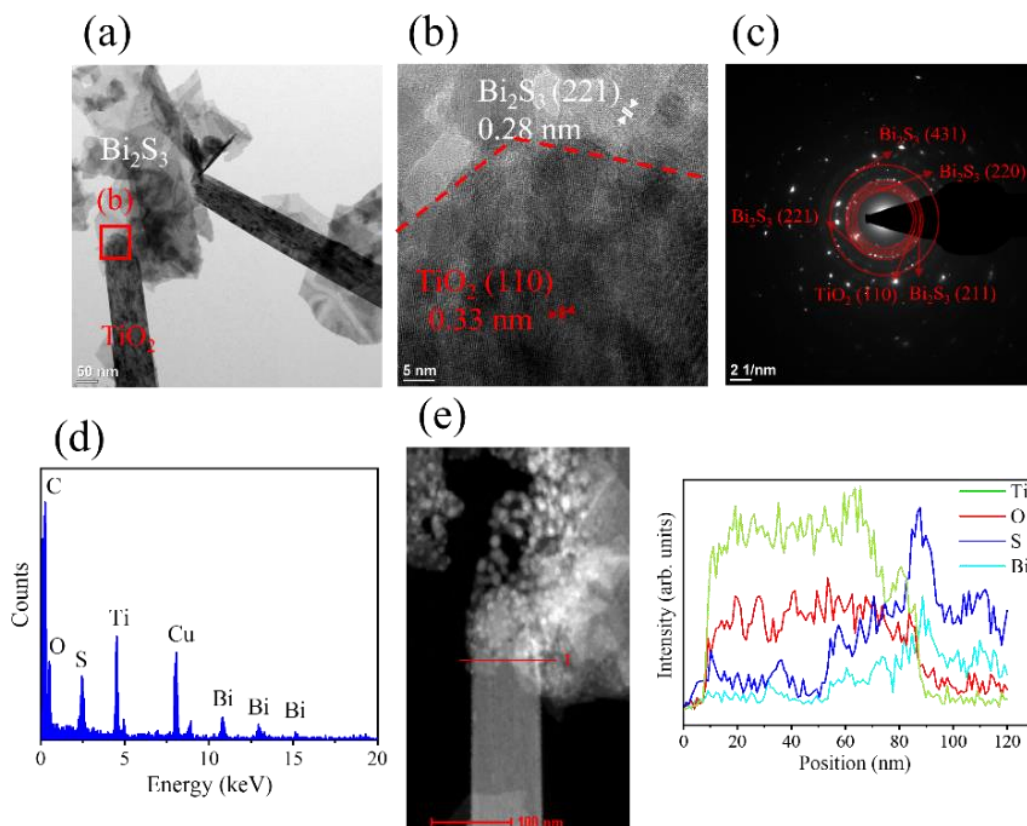
Figure 4. (**a**) Low magnification TEM image of BT-1. (**b**) HRTEM image taken from the local region of the sample in (**a**). (**c**) The SAED pattern of BT-1 in (**a**). (**d**) EDS spectrum taken from the sample in (**a**). (**e**) EDS line-scanning profiles across the composite.

Figure 5a shows the low-magnification TEM image of the BT-3 structure scratched from the sample. The sidewall of the composite showed an undulated feature because of the decoration of Bi_2S_3 crystals. However, a broken top region of the structure was observed in Figure 5a. Because the preparation of TEM sample with a scratched off method will destroy the integrity of the BT-3 composite, the distinct two-layered structure of the BT-3 composite is not observed herein, as revealed in the aforementioned SEM observation. Figure 5b displays the HRTEM image taken from the red square region in Figure 5a. The distinct lattice fringes with a distance of approximately 0.28 nm are associated with the interplanar spacing of Bi_2S_3 (2 2 1). Figure 5c demonstrates the EDS spectrum taken from the nanostructure in Figure 5a. In addition to Cu and C originated from the TEM grid, the Ti, O, Bi, and S are the main constituent elements in this composite structure, which proves that TiO_2 and Bi_2S_3 phases coexist in the composite structure. Figure 5d presents a low-magnification image of the scratched nanowire structure from BT-3 sample. The nanowire has the diameter of 23 nm, and the surface is smooth. The nanowire shows a little bent state. Figure 5e shows the HRTEM image taken from the red square in Figure 5d. The distinct and ordered lattice fringes shows the single crystalline quality of the Bi_2S_3 nanowire. Similarity, a distinguishable Bi_2S_3 (2 2 1) lattice image in the one-dimensional Bi_2S_3 crystal in an orthorhombic structure has been shown in WO_3/Bi_2S_3 composite synthesized via chemical bath deposition [21]. Figure 5f shows the EDS spectrum taken from the single Bi_2S_3 nanowire, where the EDS spectrum indicates high purity of Bi_2S_3 composition of the nanowire.
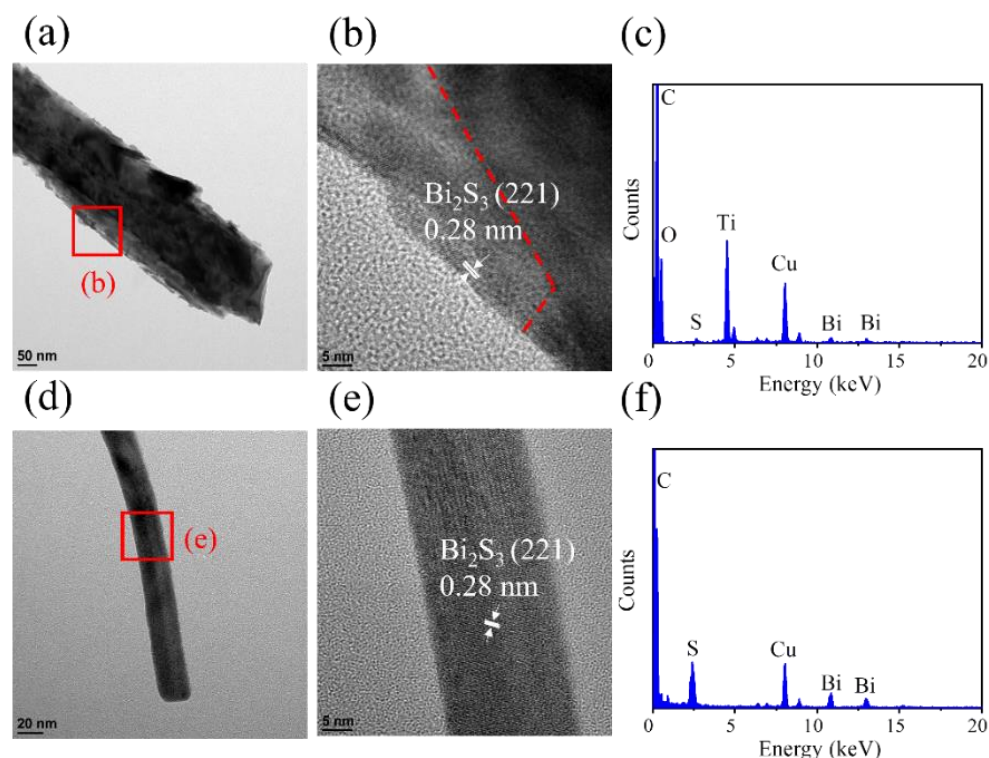
Figure 5. (**a**) Low-magnification TEM image of scratched BT-3. (**b**) HRTEM image taken from the local region of the sample in (**a**). (**c**) The EDS spectrum of BT-3 in (**a**). (**d**) Low magnification TEM image of Bi_2S_3 nanowire scratched from BT-3. (**e**) HRTEM image taken from the local regions of the sample in (**d**). (**f**) The EDS spectrum of Bi_2S_3 nanowire in (**d**).

Figure 6 shows the characteristic XPS spectral lines of various samples. The main constituent elements of Bi, S, Ti, and O are detected in BT-1, BT-3, and BT-5, supporting the existence of Bi_2S_3 and TiO_2 in the composite structure. Moreover, the relatively weak Ti signals from the spectra in comparison with that of the Bi signals, revealing the capping layer of Bi_2S_3 phase on the TiO_2 template for the test samples, and this spectral feature has

widely been observed in the composite structure, having obvious layering characteristics [9]. In addition to the C signal that originated from the sample contamination on exposure to ambient air, no impurity was detected in the as-synthesized samples. In order to further investigate the elemental binding states of the Bi_2S_3 capping layer, the XPS narrow scan spectra of Bi 4f for BT-1, BT-3, and BT-5 are displayed in Figure 7a–c, respectively. Two sharp and distinct peaks centered at approximately 157.3 eV and 162.6 eV, which are assigned to Bi $4f_{7/2}$ and Bi $4f_{5/2}$ of Bi_2S_3, respectively [22]. The tiny peak located between the two distinct characteristic peaks of Bi 4f is originated from S 2p. The binding energies of Bi 4f core-level peaks corresponded to the characteristic binding state of Bi^{3+} in the Bi_2S_3, revealing the well formation of the Bi_2S_3 phase through vulcanizing the Bi_2O_3 layer. No metallic Bi or Bi_2O_3 appeared after vulcanization.
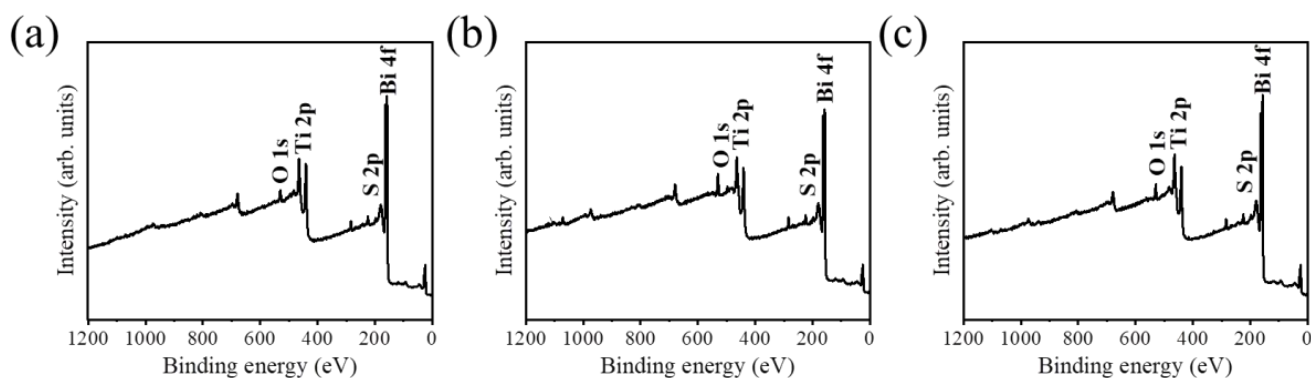
Figure 6. XPS survey scan spectra: (**a**) BT-1, (**b**) BT-3, and (**c**) BT-5.
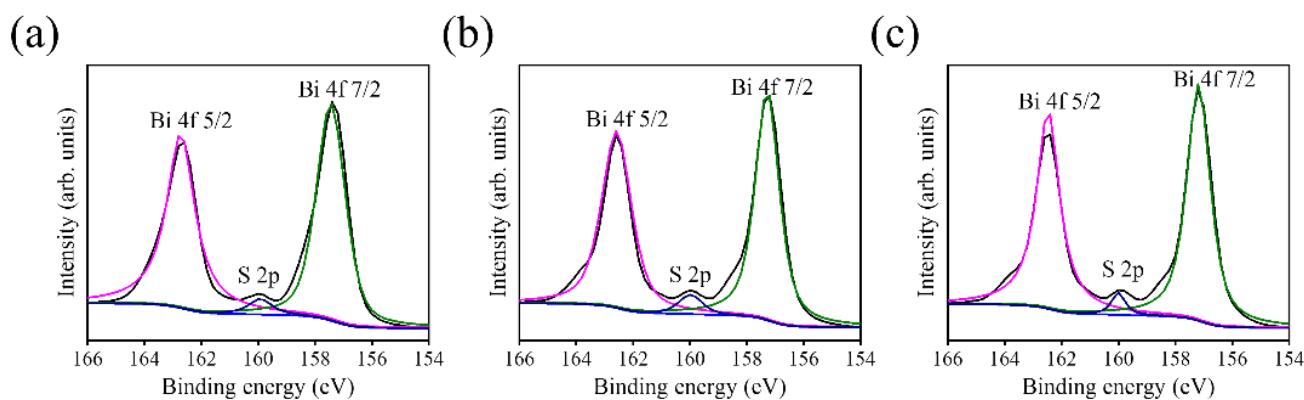
Figure 7. XPS analysis of narrow scan Bi 4f spectra: (**a**) BT-1, (**b**) BT-3, and (**c**) BT-5.

Notably, the narrow scan spectra of S 2p region of BT-1, BT-3, and BT-5 in Figure 8 reveal the characteristic peaks centered at approximately 162.6 eV and 160.1 eV, which are assigned to S $2p_{1/2}$ and S $2p_{3/2}$, respectively. The S 2p binding energies herein associated with the aforementioned Bi 4f binding states evidenced the formation of Bi-S bonds in the capping layer synthesized via the given vulcanization processes in this study [23].

A comparison of the UV-vis absorption spectra of TiO_2 template and various TiO_2-Bi_2S_3 samples are displayed in Figure 9a. The absorption of the TiO_2 template is mainly in the UV light range. The decoration of Bi_2S_3 extends the absorption range of the TiO_2 template to the visible light range because of the narrow energy gap of Bi_2S_3. This is consistent with the feature of optical absorption spectra for Bi_2S_3 nanorod/TiO_2 nanoplate composites [24]. Moreover, in the previous TiO_2/Bi_2S_3 core–shell nanowire arrays synthesized via a successive ionic layer adsorption and reaction method, the absorption of the composite extends to cover the visible light range, and the decoration of Bi_2S_3 phase increases the light absorption ability of the pristine TiO_2 nanowires [8]. Notably, the band gap energies of the pristine TiO_2 and Bi_2S_3 are evaluated in Figure 9b,c, respectively, from Tauc plots based on

Kubelka–Munk function [25]. The TiO_2 has a band gap energy of approximately 3.02 eV, and the band gap energy of the reference Bi_2S_3 derived from the sputtering deposited Bi_2O_3 layer and then vulcanized using 0.1 M thiourea is approximately 1.3 eV. Based on the evaluated band gap energy, the construction of the TiO_2/Bi_2S_3 heterostructure herein improves the light harvesting ability.
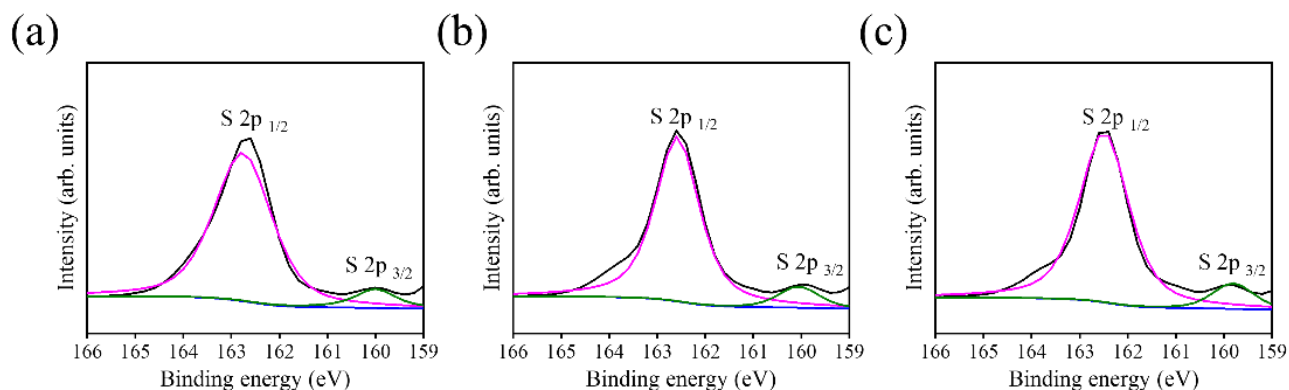
Figure 8. XPS analysis of narrow scan S 2p spectra: (**a**) BT-1, (**b**) BT-3, and (**c**) BT-5.
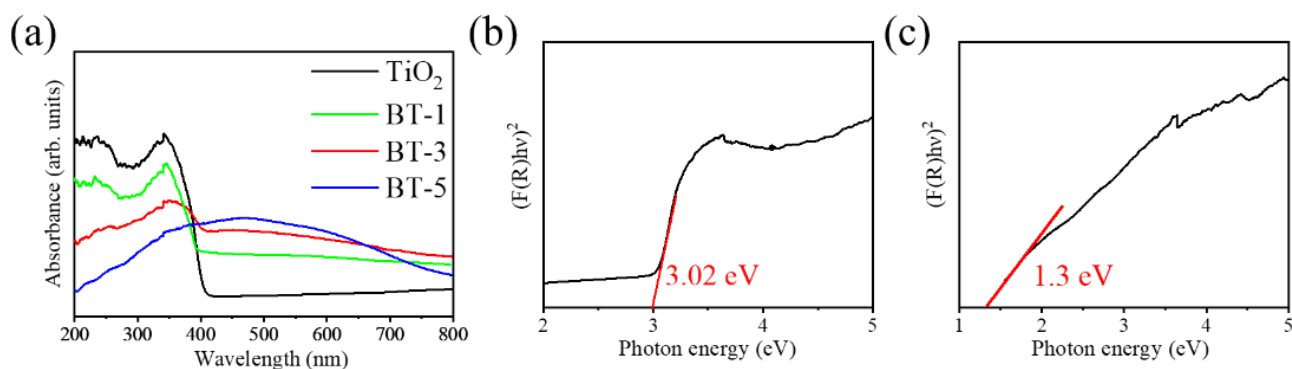
Figure 9. (**a**) UV–vis absorbance spectra of various samples. Band gap evaluation of (**b**) pristine TiO_2 and (**c**) pristine Bi_2S_3.

Figure 10a shows the transient photocurrent performance of various photoelectrodes under repeated on/off irradiation cycles at 0.5 V (vs. Ag/AgCl). It is known that the transient photocurrent performance is highly associated with the photoresponse, charge carrier transport speed, charge carrier separation efficiency, and charge carrier recombination rate of samples. When the light is on, the photocurrent densities of all samples swiftly rise to a stable value of 0.12, 0.81, 0.93, and 0.47 mA/cm^2 for TiO_2, BT-1, BT-3, and BT-5, respectively. When the light is off, the photocurrent densities of the samples drop to their initial dark current density value instantaneously. Such a fast rise and fall process of the photocurrents indicates that carrier transport and separation in the prepared photoelectrodes proceed quickly [11]. Furthermore, the photoresponse of the BT-3 increased approximately three times higher than that of the TiO_2 template. The BT-1 and BT-5 also exhibited enhanced photoresponses in comparison with the TiO_2 template. Among various composite structure, the BT-3 has the highest photocurrent response, indicating it has the lowest photogenerated electron/hole recombination rate. By contrast, the BT-5 exhibits a lower photocurrent response among various composites. This might be attributed to the following reason. Substantially excessive Bi_2S_3 deposition leads to an increase in the number of recombination centers, and as a result, a decrease in photocurrent density has been observed due to the loss of photogenerated electrons [15]. The results herein prove that decoration of Bi_2S_3 crystals onto the TiO_2 template can effectively improve the photoinduced charge separation efficiency of the TiO_2 template, resulting in more efficient charge migration and

higher photocurrent density of the TiO_2-Bi_2S_3 composite structure. A similar improved transient photocurrent performance because of decoration of visible light sensitizer onto the wide band gap semiconductor with a suitable band alignment has been demonstrated in TiO_2-Bi_2O_3 and ZnO-Sn_2S_3 heterostructures [11,25]. Figure 10b presents the Nyquist plots of various photoelectrodes. The semicircular radius of the Nyquist plots can reflect the charge transfer resistance of the photoelectrode materials. As show in Figure 10b, the arc radius of the TiO_2-Bi_2S_3 composites herein are smaller than that of the TiO_2 template, revealing that formation of TiO_2/Bi_2S_3 heterojunction is beneficial for interfacial charge transfer. Comparatively, BT-3 has the smallest radius of the Nyquist curve among various samples. The possible equivalent circuits shown in Figure 10c are used to fit the EIS Nyquist results, where Rs, R1, R2, and CPE represent the solution resistance, semiconductor depletion layer resistance, charge transfer resistance, and chemical capacitance, respectively [26]. Herein, the R2 is evaluated from the fitting results of the Nyquist plots at the low frequency region. The R2 values of the pristine TiO_2, BT-1, BT-3, and BT-5 are 3500, 583.3, 463.4, and 925 Ω, respectively. The BT-3 exhibited the smallest R2 value. As the vulcanization duration was further prolonged, a larger size of Bi_2S_3 crystallites deposition occurred, which might prolong the electron diffusion path in the BT-5 composite, resulting a larger R2 value among various composites. Notably, charge transfer resistances of the BT-1, BT-3, and BT-5 are much lower than that of TiO_2. This indicates that decoration of Bi_2S_3 onto the TiO_2 could effectively reduce the photoinduced charge transfer resistance of the TiO_2 template and enhance the separation efficiency of charge carriers. Both the transient photocurrent and Nyquist plot results herein support an effective separation of photogenerated electron–hole pairs and faster interfacial charge transfer occurred on the BT-3 interface, which might lead to the enhanced photocatalytic performance.
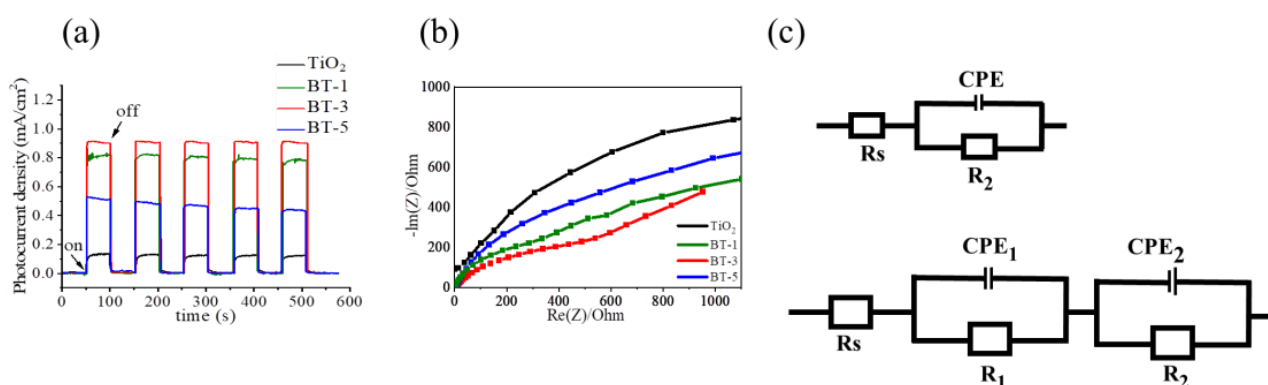
Figure 10. (**a**) Photocurrent density versus time curves of various samples at 0.5 V vs. Ag/AgCl under chopped illumination. (**b**) Nyquist plot of various samples at an open-circuit potential under illumination (**c**) Possible equivalent circuits used to fit R2 value of the pristine TiO_2 and TiO_2-Bi_2S_3 composite.

Figure 11 shows the Mott–Schottky (M–S) plots of TiO_2, Bi_2S_3, and TiO_2-Bi_2S_3 composites performed at 1 kHz. All the samples were measured with a positive slope in the M–S plots, revealing an n-type nature of the composed semiconductors. The flat band potential (E_{fb}) of various samples can be calculated from the x intercept of the linear region in the M–S plots according to the M–S equation [27]. Furthermore, the normal hydrogen electrode (NHE) potential can be converted from the Ag/AgCl reference electrode as NHE = V(Ag/AgCl)—0.197 V. The E_{fb} of TiO_2 and Bi_2S_3 referenced samples are −0.21 and −0.45 V vs. NHE, respectively. Comparatively, the flat band potential of the TiO_2-Bi_2S_3 composites has a negative shift compared to the TiO_2 template as exhibited in Figure 11c–e. Moreover, the tangent slope in the linear region of the M–S plots for the TiO_2-Bi_2S_3 composites is smaller than the TiO_2 template, demonstrating the decoration of Bi_2S_3 crystallites onto the TiO_2 template increases carrier concentration and reduce the charge recombination rate of the composites. A more negative shift of the flat band potential with respective to TiO_2 template is observed for the BT-3 among various TiO_2-Bi_2S_3 composites; moreover,

the smaller tangent slop in the linear region of the M–S plot was observed for the BT-3. These reveal a superior electronic property of the BT-3 than that of other TiO_2-Bi_2S_3 composites. It has been shown that the crystallite size and number of visible-light sensitizers affect the photoinduced charge separation efficiency of the visible-light sensitizer-decorated TiO_2 [28]. Moreover, the crystal quality of the semiconductor has been proved to affect its photoactivity [29]. The BT-3 because of suitable Bi_2S_3 crystallite quality and size shows the superior photogenerated carrier density and effective interface transfer ability among various composites in this study.
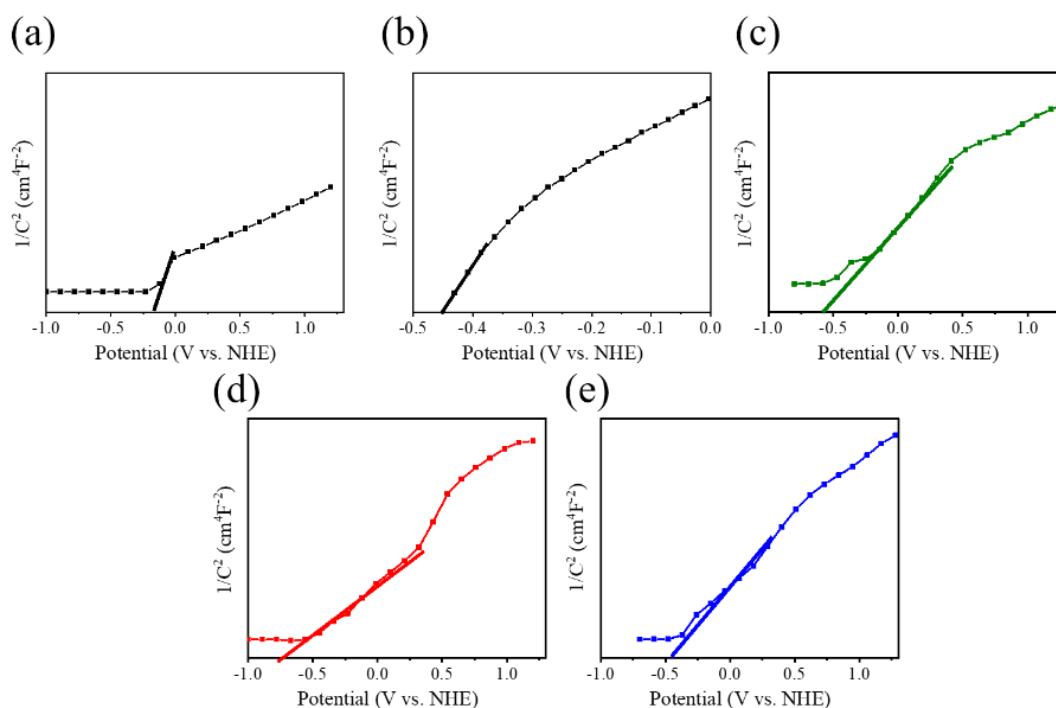
Figure 11. Mott–Schottky plots of various samples: (**a**) pristine TiO_2, (**b**) pristine Bi_2S_3, (**c**) BT-1, (**d**) BT-3, and (**e**) BT-5.

Figure 12a shows the photodegradation level of various photocatalysts towards RhB solution. The percentage of photodegradation was calculated using the $C/C_o = I_t/I_o$. The C_o and C are the initial and residual concentration of the RhB solution at $t = 0$ and at irradiation duration t, respectively, and can be evaluated from the intensity variation of absorbance spectra of the RhB solution with and without photocatalytic reaction [30]. Figure 12a demonstrates that the BT-1, BT-3, BT-5, and TiO_2 degrades 60.3%, 65.6%, 50.8%, and 36.1% of RhB solution, respectively, after 30 min irradiation. Furthermore, the degradation level of RhB solution reached 77.8%, 87.2%, 71.2%, and 57.1% after 60 min irradiation for the BT-1, BT-3, BT-5, and TiO_2, respectively. Notably, the dark balanced absorptions of various samples are also conducted to understand the initial catalysts' surface dye absorption efficiency. The C/C_o of the BT-1, BT-3, BT-5, and TiO_2 after 30 min dark balanced adsorption is 7.1%, 7.6%, 5.8%, and 4.2%, respectively. Comparatively, the BT-1 and BT-3 exhibit a slightly larger surface dye adsorption ability than that of BT-5 and TiO_2. Figure 12b demonstrates the discoloration of RhB solution with BT-3 under different irradiation durations. Apparent discoloration appeared in the RhB solution containing BT-3 with an increased irradiation duration. To quantitatively compare the photocatalytic activity of the as-prepared photocatalyst samples, the photodegradation data were fitted to the pseudo-first-order kinetics equation: $\ln(C_o/C) = kt$, where k is the apparent first-order rate constant [4]. Figure 12c presents the plot of $\ln(C_o/C)$ versus t for various samples. The higher k value is observed for the TiO_2-Bi_2S_3 composites than that of pristine TiO_2. Moreover, the BT-3 demonstrates the highest k value of 0.03274 min^{-1} among various samples, confirming the higher photocatalytic activity of BT-3 composite. The suitable

morphology and decoration content of Bi_2S_3 crystallites on the TiO_2 template might account for the observed result. This has also been supported by visible-light CuO sensitizer decorated ZnO composite photocatalysts that crystal morphology and content of the CuO substantially affect the photocatalytic activity of CuO-ZnO nanocomposites [31]. Active groups of the photocatalytic degradation reaction were explored by the addition of free radical capture agents, as exhibited in Figure 12d. Herein, benzoquinone (BQ, $\cdot O_2^-$ radical scavenger), tertiary butyl alcohol (t-BuOH, $\cdot OH$ radical scavenger), and EDTA-2Na (EDTA-2Na, h^+ radical scavenger) are used to explore the active groups of the photocatalytic degradation reaction. Notably, the photocatalytic efficiency of RhB solution with BT-3 was significantly inhibited after adding BQ, indicating that $\cdot O_2^-$ is the main active substance for RhB degradation. Furthermore, the results herein reveal that a single scavenger could not completely prevent the dye degradation, and the h^+ and $\cdot OH$ also contribute some degrees of photodegradation towards RhB dyes.
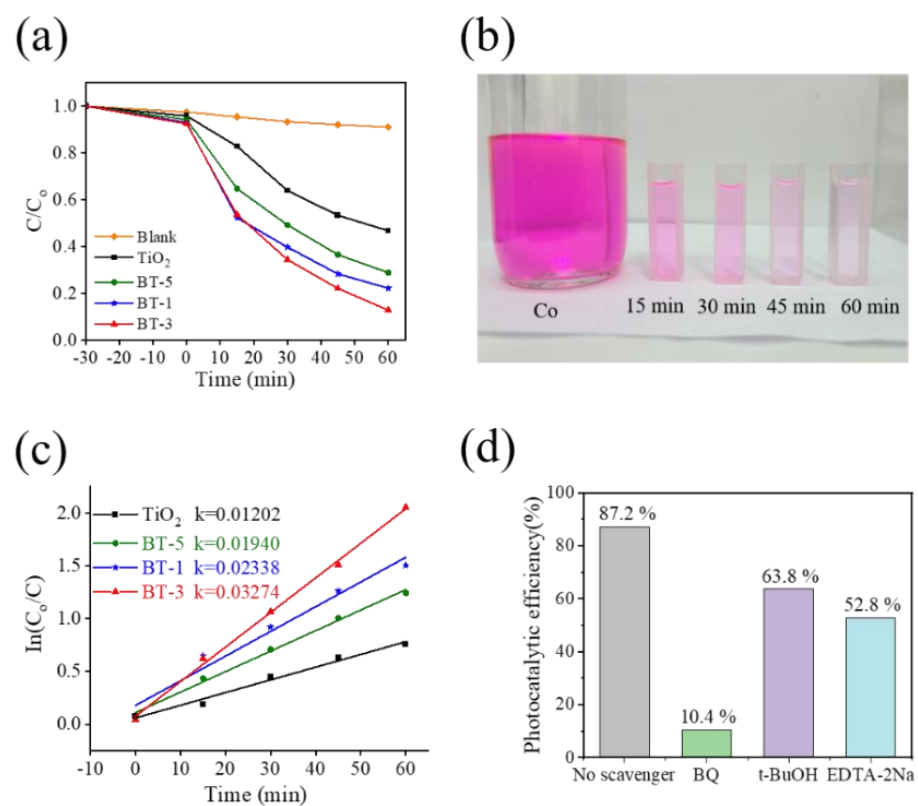
Figure 12. (**a**) C/Co versus irradiation duration plot. (**b**) Discoloration of RhB solution with BT-3 under different irradiation durations. (**c**) ln (Co/C) versus irradiation duration plot. (**d**) The photocatalytic performance after adding various scavengers in BT-3/RhB solution.

In the M-S analysis, the flat band potentials of the TiO_2 and Bi_2S_3 are -0.21 and -0.45 eV, respectively. Furthermore, the E_{CB} bottoms of the TiO_2 and Bi_2S_3 can be evaluated to be -0.31 and -0.55 eV, respectively [32]. The valence band (VB) positions of the TiO_2 and Bi_2S_3 are evaluated to be 2.71 and 0.75 eV, respectively. According to the band structures of TiO_2 and Bi_2S_3, there are two possible migration mechanisms of photoinduced charge carriers in the TiO_2/Bi_2S_3 heterojunction as shown in Figure 13. However, the potential of $O_2/\cdot O_2^-$ is -0.33 eV, which is more negative than CB of TiO_2, and CB electrons are not easy to reduce O_2. At the same time, the photoinduced holes on Bi_2S_3 VB cannot oxidize H_2O to produce $\cdot OH$ radicals, because the VB edge potential of Bi_2S_3 is more negative than the potential of H_2O/OH (2.27 V), as shown in Figure 13a. Based on the aforementioned discussions, type II photodegradation mechanism is not suitable for the as-synthesized TiO_2-Bi_2S_3 composites in this study. By contrast, a direct Z-scheme mechanism

over the TiO_2/Bi_2S_3 heterostructure can be proposed in Figure 13b. Upon irradiation, TiO_2/Bi_2S_3 absorbs light greater than its band gap, electron-hole pairs are generated (Equations (1) and (2)), and RhB will also be excited to RhB* by light irradiation at the same time (Equation (3)). The RhB* injects electrons into the CB of Bi_2S_3 (Equation (4)). A similar phenomenon of electron injection from RhB* to the TiO_2 CB has been proposed in the literature [33]. The electrons in the TiO_2 CB position could migrate to the Bi_2S_3 VB, resulting in the effective separation of photoinduced charge carriers (Equation (5)). The RhB^+ reacts with adsorbed dye to form intermediate products by the photosensitization process (Equation (6)). Parts of the holes in the TiO_2 VB will react with the intermediate product to degrade RhB dyes (Equation (7)). Moreover, the residual photoinduced holes in the TiO_2 VB will react with the H_2O molecules to generate the ·OH radicals (Equation (8)), and the electrons are gathered on Bi_2S_3 CB to produce $·O_2^-$ radicals (Equation (9)) [34]. Therefore, the RhB dyes are effectively photodegraded with BT-3 under irradiation (Equation (10)). A similar Z-scheme mechanism is shown in other TiO_2-based composite systems decorated with visible-light sensitizers [35–37].

$$TiO_2 + h\upsilon \rightarrow TiO_2\ e^-(CB) + TiO_2\ h^+(VB) \tag{1}$$

$$Bi_2S_3 + h\upsilon \rightarrow Bi_2S_3\ e^-(CB) + Bi_2S_3\ h^+(VB) \tag{2}$$

$$RhB + h\upsilon \rightarrow\ RhB^*(LUMO) +\ RhB^+(HOMO) \tag{3}$$

$$RhB^*(LUMO) + Bi_2S_3\ e^-(CB) \rightarrow Bi_2S_3\ total\ e^-(CB) \tag{4}$$

$$TiO_2\ e^-(CB) + Bi_2S_3\ h^+(VB) \rightarrow recombination \tag{5}$$

$$RhB^+(HOMO) + RhB_{(abs)} \rightarrow Intermediate \tag{6}$$

$$Intermediate + TiO_2\ h^+(VB) \rightarrow degradation\ products \tag{7}$$

$$TiO_2\ h^+(VB) + H_2O \rightarrow\ ·OH \tag{8}$$

$$Bi_2S_3\ e^-(CB) + O_2 \rightarrow\ ·O_2^- \tag{9}$$

$$RhB +\ ·O_2^- \rightarrow degradation\ products \tag{10}$$
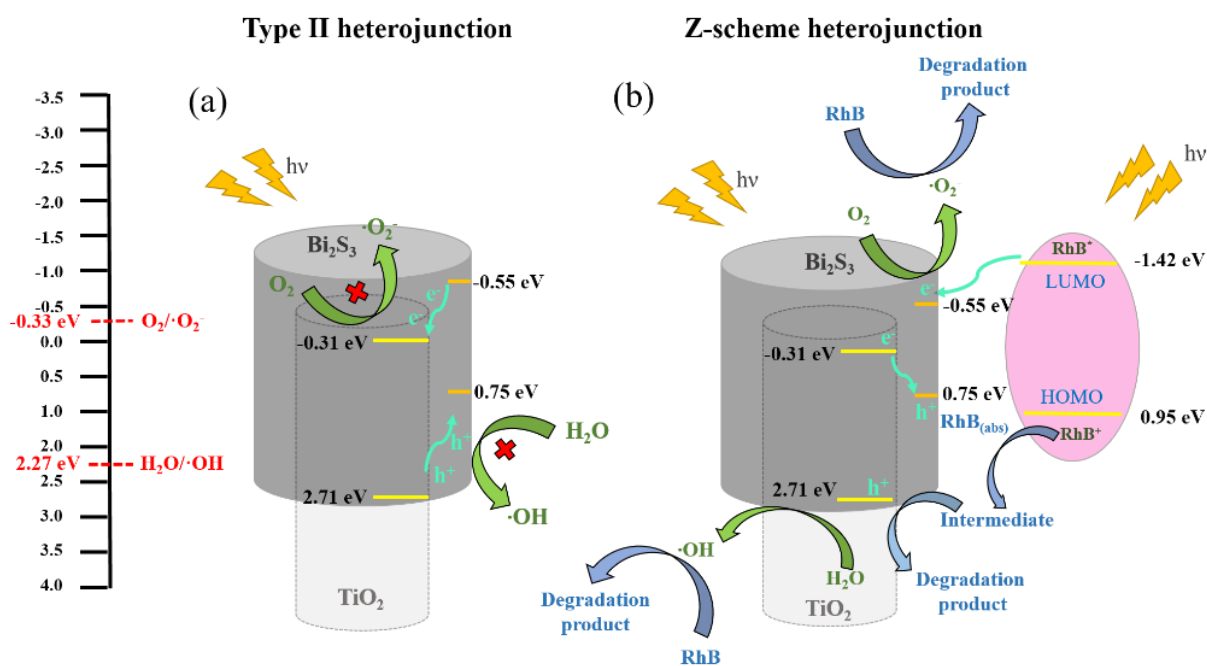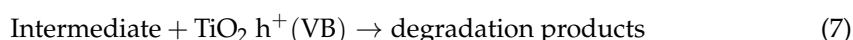
Figure 13. Schematic diagrams of the photogenerated electron–hole separation process for TiO_2/Bi_2S_3 composites: (**a**) Type II heterojunction and (**b**) Z-scheme heterojunction.

4. Conclusions

TiO_2 nanorod array coated with Bi_2O_3 layer was used to vulcanize to form TiO_2-Bi_2S_3 composites with various morphologies. The hydrothermal vulcanization duration profoundly affects the microstructure, optical properties, and photoactivity of TiO_2-Bi_2S_3 composites. The decorated Bi_2S_3 crystals changed the morphology from filament, nanowire to nanorod with an increased vulcanization duration from 1, 3, and 5 h, respectively. The decoration of Bi_2S_3 crystals enhanced the light absorption capacity of the TiO_2 nanorod template. The improved photodegradation performance of the composites can be reasonably attributed to the construction of the direct Z-scheme heterojunction between the TiO_2 and Bi_2S_3. This study demonstrates that design of TiO_2-Bi_2S_3 composites with suitable morphology of decorated Bi_2S_3 crystals can tune the photoactivity of the composites, and the findings in this study may be of great value for the development of oxide-sulfide composites for ideal photosensitive device applications.

Author Contributions: Methodology, Y.-C.L. and S.-Y.Y.; formal analysis, S.-Y.Y. and B.-Y.C.; investigation, S.-Y.Y. and B.-Y.C.; writing—original draft preparation, Y.-C.L. and S.-Y.Y.; supervision, Y.-C.L. All authors have read and agreed to the published version of the manuscript.

Data Availability Statement: Not applicable.

Conflicts of Interest: The authors declare no conflict of interest.

References

1. Wei, L.; Li, F.; Hu, S.; Li, H.; Chi, B.; Pu, J.; Jian, L. CdS Quantum Dot-Sensitized Vertical TiO_2 Nanorod Arrays by a Simple Linker-Assisted SILAR Method. *J. Am. Ceram. Soc.* **2015**, *98*, 3173–3178. [CrossRef]
2. Yang, H.; Chen, J.; Zuo, Y.; Zhang, M.; He, G.; Sun, Z. Enhancement of photocatalytic and photoelectrochemical properties of BiOI nanosheets and silver quantum dots co-modified TiO_2 nanorod arrays. *J. Am. Ceram. Soc.* **2019**, *102*, 5966–5975. [CrossRef]
3. Wang, L.-L.; Wang, R.; Feng, L.; Liu, Y. Coupling TiO_2 nanorods with g-CN using modified physical vapor deposition for efficient photoelectrochemical water oxidation. *J. Am. Ceram. Soc.* **2020**, *103*, 6272–6279. [CrossRef]
4. Liang, Y.-C.; Zhao, W.-C. Morphology-dependent photocatalytic and gas-sensing functions of three-dimensional TiO_2–ZnO nanoarchitectures. *CrystEngComm* **2020**, *22*, 7575–7589. [CrossRef]
5. Liang, Y.-C.; Zhao, W.-C. Crystal Growth and Design of Disk/Filament ZnO-Decorated 1D TiO_2 Composite Ceramics for Photoexcited Device Applications. *Nanomaterials* **2021**, *11*, 667–678.
6. Lin, J.; Liu, X.; Zhu, S.; Chen, X. TiO_2 nanotube structures for the enhancement of photon utilization in sensitized solar cells. *Nanotechnol. Rev.* **2015**, *4*, 209–238. [CrossRef]
7. Lozano, H.; Devis, S.; Aliaga, J.; Alegría, M.; Guzmán, H.; Villarroel, R.; Benavente, E.; González, G. Two-Dimensional Titanium Dioxide–Surfactant Photoactive Supramolecular Networks: Synthesis, Properties, and Applications for the Conversion of Light Energy. *Int. J. Mol. Sci.* **2022**, *23*, 4006. [CrossRef]
8. Fawzi, T.; Rani, S.; Roy, S.C.; Lee, H. Photocatalytic Carbon Dioxide Conversion by Structurally and Materially Modified Titanium Dioxide Nanostructures. *Int. J. Mol. Sci.* **2022**, *23*, 8143. [CrossRef]
9. Meng, A.; Zhu, B.; Zhong, B.; Zhang, L.; Cheng, B. Direct Z-scheme TiO_2/CdS hierarchical photocatalyst for enhanced photocatalytic H_2-production activity. *Appl. Surf. Sci.* **2017**, *422*, 518–527. [CrossRef]
10. Lee, S.S.; Bai, H.; Liu, Z.; Sun, D.D. Novel-structured electrospun TiO_2/CuO composite nanofibers for high efficient photocatalytic cogeneration of clean water and energy from dye wastewater. *Water Res.* **2013**, *47*, 4059–4073. [CrossRef] [PubMed]
11. Liang, Y.-C.; Chiang, K.-J. Coverage Layer Phase Composition-Dependent Photoactivity of One-Dimensional TiO_2-Bi_2O_3 Composites. *Nanomaterials* **2020**, *10*, 1005. [CrossRef]
12. Liang, Y.-C.; Liu, Y.-C. Microstructures and photodegradation performance toward methylene orange of sputtering-assisted decoration of $ZnFe_2O_4$ crystallites onto TiO_2 nanorods. *Nanomaterials* **2019**, *9*, 205. [CrossRef]
13. Ai, G.; Mo, R.; Chen, Q.; Xu, H.; Yang, S.; Li, H.; Zhong, J. TiO_2/Bi_2S_3 core–shell nanowire arrays for photoelectrochemical hydrogen generation. *RSC Adv.* **2015**, *5*, 13544–13549. [CrossRef]
14. Liu, C.; Yang, Y.; Li, W.; Li, J.; Li, Y.; Chen, Q. A novel Bi_2S_3 nanowire@ TiO_2 nanorod heterogeneous nanostructure for photoelectrochemical hydrogen generation. *Chem. Eng. J.* **2016**, *302*, 717–724. [CrossRef]
15. Ahmad, A.; Tezcan, F.; Yerlikaya, G.; Paksoy, H.; Kardaş, G. Three dimensional rosette-rod TiO2/Bi2S3 heterojunction for enhanced photoelectrochemical water splitting. *J. Alloys Compd.* **2021**, *868*, 159133. [CrossRef]
16. Li, X.; Han, X.; Zhu, D.; Chen, Y.; Li, L.; Ren, F.; Huang, J. Hydrothermal method deposition of TiO2/Bi2S3 composite film for solar cell photoanode. *Mater. Res. Express* **2019**, *6*, 055910. [CrossRef]

17. Liang, Y.-C.; Li, T.-H. Controllable morphology of Bi_2S_3 nanostructures formed via hydrothermal vulcanization of Bi_2O_3 thin-film layer and their photoelectrocatalytic performances. *Nanotechnol. Rev.* **2022**, *11*, 284–297. [CrossRef]

18. Sun, B.; Feng, T.; Dong, J.; Li, X.; Liu, X.; Wu, J.; Ai, S. Green synthesis of bismuth sulfide nanostructures with tunable morphologies and robust photoelectrochemical performance. *Cryst. Eng. Comm.* **2019**, *21*, 1474–1481. [CrossRef]

19. Liang, Y.-C.; Xu, N.-C. Synthesis of TiO_2–ZnS nanocomposites via sacrificial template sulfidation and their ethanol gas-sensing performance. *RSC Adv.* **2018**, *8*, 22437–22446. [CrossRef] [PubMed]

20. Chen, L.; He, J.; Yuan, Q.; Liu, Y.; Au, C.T.; Yin, S.F. Environmentally benign synthesis of branched Bi_2O_3–Bi_2S_3 photocatalysts by an etching and re-growth method. *J. Mater. Chem. A* **2015**, *3*, 1096–1102. [CrossRef]

21. Wang, Y.; Tian, W.; Chen, L.; Cao, F.; Guo, J.; Li, L. Three-dimensional WO_3 nanoplate/Bi_2S_3 nanorod heterojunction as a highly efficient photoanode for improved photoelectrochemical water splitting. *ACS Appl. Mater. Interfaces* **2017**, *9*, 40235–40243. [CrossRef] [PubMed]

22. Ma, G.Q.; Liu, F.S.; Wang, S.; Dang, Z.C.; Zhang, J.W.; Fu, X.J.; Hou, M.S. Preparation and characterization of Bi_2S_3/3DOM-TiO_2 for efficient photocatalytic degradation of rhodamine B. *Mater. Sci. Semicond. Process.* **2019**, *100*, 61–72. [CrossRef]

23. Xu, F.; Xu, C.; Chen, H.; Wu, D.; Gao, Z.; Ma, X.; Zhang, Q.; Jiang, K. The synthesis of Bi_2S_3/2D-Bi_2WO_6 composite materials with enhanced photocatalytic activities. *J. Alloys Compd.* **2019**, *780*, 634–642. [CrossRef]

24. Huang, G.; Zhang, J.; Jiang, F.; Zhang, Z.; Zeng, J.; Qi, X.; Shen, Z.; Wang, H.; Kong, Z.; Ji, Z.; et al. Excellent photoelectrochemical activity of Bi_2S_3 nanorod/TiO_2 nanoplate composites with dominant {001} facets. *J. Solid State Chem.* **2020**, *281*, 121041. [CrossRef]

25. Liang, Y.C.; Lung, T.W.; Xu, N.C. Photoexcited properties of tin sulfide nanosheet-decorated ZnO nanorod heterostructures. *Nanoscale Res. Lett.* **2017**, *12*, 1–8. [CrossRef]

26. Guan, Z.C.; Wang, X.; Jin, P.; Tang, Y.Y.; Wang, H.P.; Song, G.L.; Du, R.G. Enhanced photoelectrochemical performances of ZnS-Bi_2S_3/TiO_2/WO_3 composite film for photocathodic protection. *Corros. Sci.* **2018**, *143*, 31–38. [CrossRef]

27. Hao, C.; Wang, W.; Zhang, R.; Zou, B.; Shi, H. Enhanced photoelectrochemical water splitting with TiO_2@Ag_2O nanowire arrays via p-n heterojunction formation. *Sol. Energy Mater. Sol. Cells* **2018**, *174*, 132–139. [CrossRef]

28. Wang, Q.; Liu, Z.; Jin, R.; Wang, Y.; Gao, S. SILAR preparation of Bi_2S_3 nanoparticles sensitized TiO_2 nanotube arrays for efficient solar cells and photocatalysts. *Sep. Purif. Technol.* **2019**, *210*, 798–803. [CrossRef]

29. Liang, Y.-C.; Chang, C.-W. Preparation of orthorhombic WO_3 thin films and their crystal quality-dependent dye photodegradation ability. *Coatings* **2019**, *9*, 90. [CrossRef]

30. Liang, Y.-C.; Chiang, K.-J. Design and tuning functionality of rod-like titanium dioxide–nickel oxide composites via a combinational methodology. *Nanotechnology* **2020**, *31*, 195709. [CrossRef]

31. Das, S.; Srivastava, V.C. An overview of the synthesis of CuO-ZnO nanocomposite for environmental and other applications. *Nanotechnol. Rev.* **2018**, *7*, 267–282. [CrossRef]

32. Kavan, L.; Vlckova Zivcova, Z.; Zlamalova, M.; Zakeeruddin, S.M.; Grätzel, M. Electron-selective layers for dye-sensitized solar cells based on TiO_2 and SnO_2. *J. Phys. Chem. C* **2020**, *124*, 6512–6521. [CrossRef]

33. Pan, L.; Zou, J.J.; Liu, X.Y.; Liu, X.J.; Wang, S.; Zhang, X.; Wang, L. Visible–light–induced photodegradation of rhodamine B over hierarchical TiO_2: Effects of storage period and water-mediated adsorption switch. *Ind. Eng. Chem. Res.* **2012**, *51*, 12782–12786. [CrossRef]

34. Zhu, L.; Li, H.; Xia, P.; Liu, Z.; Xiong, D. Hierarchical ZnO decorated with CeO_2 nanoparticles as the direct Z-scheme heterojunction for enhanced photocatalytic activity. *ACS Appl. Mater. Interfaces* **2018**, *10*, 39679–39687. [CrossRef] [PubMed]

35. Xue, Y.; Wu, Z.; He, X.; Yang, X.; Chen, X.; Gao, Z. Constructing a Z-scheme Heterojunction of Egg-Like Core@shell CdS@TiO_2 Photocatalyst via a Facile Reflux Method for Enhanced Photocatalytic Performance. *Nanomaterials* **2019**, *9*, 222. [CrossRef]

36. Zhao, W.; Yang, X.; Liu, C.; Qian, X.; Wen, Y.; Yang, Q.; Sun, T.; Chang, W.; Liu, X.; Chen, Z. Facile Construction of All-Solid-State Z-Scheme g-C_3N_4/TiO_2 Thin Film for the Efficient Visible-Light Degradation of Organic Pollutant. *Nanomaterials* **2020**, *10*, 600. [CrossRef]

37. Sharma, S.; Ibhadon, A.O.; Francesconi, M.G.; Mehta, S.K.; Elumalai, S.; Kansal, S.K.; Umar, A.; Baskoutas, S. Bi_2WO_6/C-Dots/TiO_2: A Novel Z-Scheme Photocatalyst for the Degradation of Fluoroquinolone Levofloxacin from Aqueous Medium. *Nanomaterials* **2020**, *10*, 910. [CrossRef]